J. Fluid Mech. (2014), *vol.* 747, *pp.* 119–140. © Cambridge University Press 2014
doi:10.1017/jfm.2014.110

Characteristics of air entrainment during dynamic wetting failure along a planar substrate

E. Vandre[1], M. S. Carvalho[2,†] and S. Kumar[1,†]

[1]Department of Chemical Engineering and Materials Science, University of Minnesota, Minneapolis, MN 55455, USA

[2]Department of Mechanical Engineering, Pontificia Universidade Catòlica do Rio de Janeiro, Rio de Janeiro, RJ, Brazil

(Received 2 September 2013; revised 17 February 2014; accepted 24 February 2014; first published online 14 April 2014)

Characteristic substrate speeds and meniscus shapes associated with the onset of air entrainment are studied during dynamic wetting failure along a planar substrate. Using high-speed video, the behaviour of the dynamic contact line (DCL) is recorded as a tape substrate is drawn through a bath of a glycerol/water solution. Air entrainment is identified by triangular air films that elongate from the DCL above some critical substrate speed. Meniscus confinement within a narrow gap between the substrate and a stationary plate is shown to delay air entrainment to higher speeds for a wide range of liquid viscosities, expanding upon the findings of Vandre, Carvalho & Kumar (*J. Fluid Mech.*, vol. 707, 2012, pp. 496–520). A pressurized liquid reservoir controls the meniscus position within the confinement gap. It is found that liquid pressurization further postpones air entrainment when the meniscus is located near a sharp corner along the stationary plate. Meniscus shapes recorded near the DCL demonstrate that operating conditions influence the size of entrained air films, with smaller films appearing in the more viscous solutions. Regardless of size, air films become unstable to thickness perturbations and ultimately rupture, leading to the entrainment of air bubbles. Recorded critical speeds and air-film sizes compare well to predictions from a hydrodynamic model for dynamic wetting failure, suggesting that strong air stresses near the DCL trigger the onset of air entrainment.

Key words: coating, contact lines, interfacial flows (free surface)

1. Introduction

Air entrainment occurs when a liquid mass fails to displace the surrounding air as it advances along a solid surface. In cases of air entrainment caused by dynamic wetting failure, air films originate at the three-phase contact line and release bubbles that are captured by the liquid flow. Air entrainment can be detrimental to industrial applications such as coating and printing processes, where bubbles lead to voids or surface irregularities in the final product (Blake & Ruschak 1997; Weinstein & Ruschak 2004; Yamamura 2007). The practical importance of this phenomenon has motivated prior experimental and theoretical studies, yet many questions remain regarding the fundamentals of air entrainment.

† Email addresses for correspondence: msc@puc-rio.br, kumar030@umn.edu

https://doi.org/10.1017/jfm.2014.110 Published online by Cambridge University Press

The enigmatic dynamic contact line (DCL) contributes many unknowns to the problem of air entrainment. Unlike a static contact line (SCL) found in a stationary system, the DCL necessarily involves transport of two fluid phases in contact with a substrate. The impact of macroscale and microscale mechanics near the DCL remains debated, as discussed in a number of reviews (de Gennes 1985; Kistler 1993; Blake 2006; De Coninck & Blake 2008; Shikhmurzaev 2008; Bonn *et al.* 2009; Yue & Feng 2011; Snoeijer & Andreotti 2013). This issue is further complicated near the limit of air entrainment, where DCL behaviour is strongly influenced by many system properties, including system geometry (Vandre, Carvalho & Kumar 2012), flow-field effects (Jacqmin 2002; Blake, Dobson & Ruschak 2004; Benkreira & Ikin 2010) and electrostatic forces (Blake, Clarke & Stattersfield 2000; Yamamura 2007).

For planar systems, air entrainment evolves from interface shapes similar to the illustration in figure 1. In this example, the capillary number $Ca = \mu U/\sigma$ characterizes dynamic wetting of a substrate moving with speed U into a liquid with viscosity μ and surface tension σ. As speed increases (larger Ca), viscous effects deform the air/liquid meniscus and move the DCL in the direction of substrate motion. At a critical speed corresponding to Ca^{crit}, the DCL becomes unstable and air films elongate into the liquid. This onset of air entrainment is often identified by a 'sawtooth' meniscus shape that results from the distribution of triangular air films along the width of the substrate (Blake & Ruschak 1979). Details of the sawtooth shape and scale depend on system parameters (e.g. liquid viscosity) in general, but descriptions within the literature have primarily been qualitative (Burley & Kennedy 1976; Severtson & Aidun 1996; Cohu & Benkreira 1998).

In a prior work, we investigated the influence of interface confinement on the critical speed associated with the onset of air entrainment (Vandre *et al.* 2012). Using an experimental apparatus in which a glycerol solution ($\mu \approx 120$ cP) is confined to a gap H (see figure 1) between a stationary surface and a rotating roll, we demonstrated that increasing confinement (smaller H) delays air entrainment to higher Ca^{crit} values. Results from a two-dimensional (2D) hydrodynamic model match the experimental trends and suggest a wetting-failure mechanism related to strong pressure gradients that pump air away from the DCL (Vandre, Carvalho & Kumar 2013). Even though the experiments make use of a scraper to remove liquid from the rotating roll, a thin liquid layer remains and effectively 'prewets' the substrate. Prewetting effects are not considered by the model which assumes an ideal substrate (i.e. smooth, chemically homogeneous and dry). Consequently, the model consistently underpredicts critical speeds recorded with the rotating-roll system. Prior to the present work, the model had not been compared against an experimental study where the substrate is completely dry before reaching the DCL.

This work presents a novel experimental study that expands upon our prior findings in three key ways. First, we find that wetting within small gaps yields high values of Ca^{crit} for a variety of glycerol/water solutions, demonstrating that meniscus confinement postpones air entrainment for liquids that span a two-order-of-magnitude range of viscosity. An initially dry polyethylene terephthalate (PET) tape is used as the substrate in the current study, eliminating any effects of substrate prewetting that were present in our previous system (Vandre *et al.* 2012). Second, liquid pressurization (using compressed air within the experimental apparatus) is found to significantly impact the dynamics of air entrainment when the meniscus is located near a sharp corner, leading to even higher critical speeds. Similar effects have been observed in high-speed fibre coating (Ravinutala & Polymeropoulos 2002; Simpkins & Kuck 2003), although to the best of the authors' knowledge, this work presents the first

https://doi.org/10.1017/jfm.2014.110 Published online by Cambridge University Press

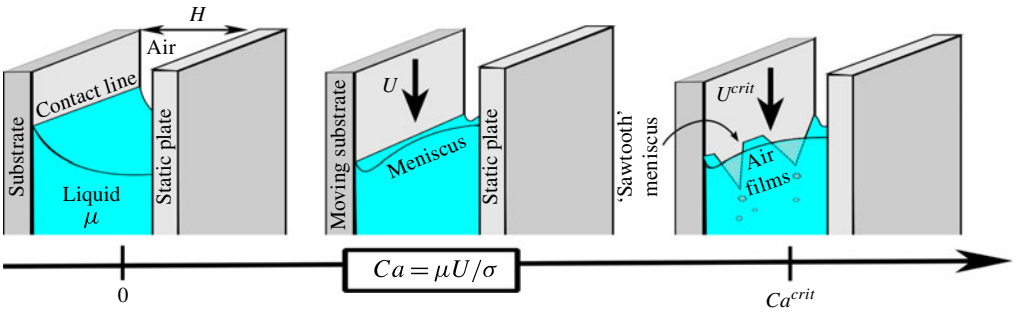


FIGURE 1. (Colour online) The stages of dynamic wetting illustrated as a function of Ca. The air/liquid meniscus is confined in a gap H between a moving substrate and a stationary plate. The meniscus becomes deformed as Ca increases, until a critical transition during the onset of air entrainment at Ca^{crit}. At this point, the contact line becomes jagged with triangular air films, yielding a 'sawtooth' meniscus shape.

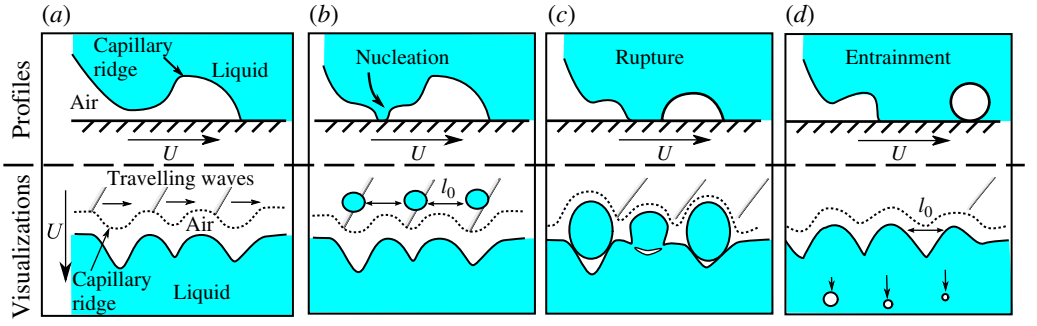


FIGURE 2. (Colour online) Idealization of the interface profiles corresponding to visualizations of air-film rupture. (*a*) Air films form with capillary ridges (shown by a dashed line in visualization panels) near the DCL. (*b*) Travelling waves nucleate liquid contacts as the air films thin near the capillary ridge. Commonly, multiple nucleation sites appear simultaneously at distances matching the wavelength l_0. (*c*) Regions of liquid contact grow until reaching the DCL. (*d*) Discrete air films pinch off from the DCL and rapidly evolve into equilibrium bubble shapes.

demonstration of air entrainment postponed via liquid pressurization in a planar geometry. Finally, close visualization of the DCL provides a new perspective on the dynamics of air entrainment. We find that the width of triangular air films that form at Ca^{crit} systematically decreases with higher liquid viscosities. Furthermore, visualizations suggest a dominant mechanism for air-film rupture, as illustrated in figure 2. This sequence portrays air-film thickness variations that propagate across the meniscus, nucleating rupture sites that ultimately cause air-bubble entrainment. Recorded critical speeds and air-film sizes compare well against predictions from the computational model used in our prior work (Vandre *et al.* 2012, 2013), further supporting a hydrodynamic mechanism for the onset of air entrainment.

This article is organized as follows. Section 2 discusses details of the experimental apparatus and methods. Section 3 presents critical speeds measured with different system geometries and solution viscosities. Section 4 shows data from image analysis of the air films formed near the DCL under different operating conditions. Section 5

https://doi.org/10.1017/jfm.2014.110 Published online by Cambridge University Press

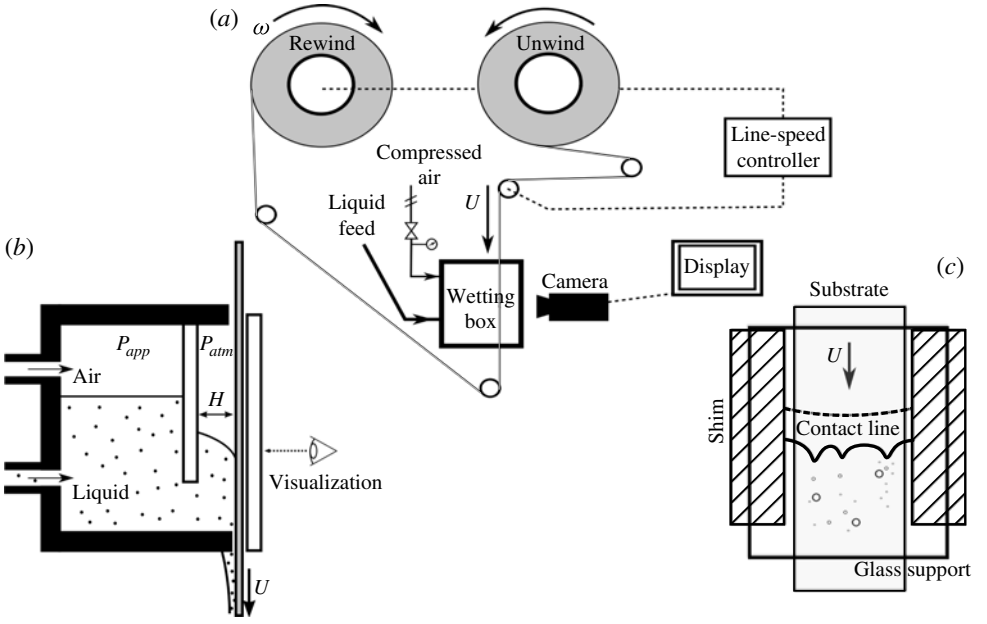


FIGURE 3. Schematic of the experimental apparatus. (*a*) Overview of the substrate's path driven by rotation of the rewind roll at angular speed ω. The line-speed controller adjusts ω through a feedback loop to maintain constant linear velocity U. (*b*) A glycerol/water solution wets the tape substrate as it passes through the wetting box. A stationary plate confines the air/liquid meniscus within a gap H. Compressed air controls the meniscus height and pressurizes the liquid (see figure 5). (*c*) A high-speed camera allows visualization of contact-line behaviour while viewing the meniscus through a glass support plate (located to the right of the substrate in panel *b*). The distance between the support and interior plates is set by shims that lie alongside the substrate. (Note that the shims are omitted from panel *b* to provide a clear view of the meniscus.)

compares experimental data to predictions from the hydrodynamic model mentioned above. Finally, § 6 summarizes our findings.

2. Experimental methods

The experimental apparatus is shown in figure 3. The apparatus features a transparent tape substrate that moves through the system as it transfers from the unwind roll to the rewind roll (see figure 3*a*). A 125 μm thick PET tape is used for all of the experiments reported in this paper. A line-speed controller (Contrex® M-Drive) adjusts the rotational speed ω of the rewind roll to maintain a set linear speed U of the tape. Along its path, the tape enters a vessel designated as the 'wetting box', where one side of the tape comes in contact with the wetting liquid and the opposite side runs along a glass support plate. Viewing through the support plate, a camera records wetting phenomena and projects real-time video to an external display.

The wetting box resembles a plunge-coating tank (approximately 10 cm in each dimension) in which the liquid reservoir is completely enclosed except for thin slots where the tape enters and exits the apparatus (see figure 3*b*). Rubber gaskets seal the exit slot and all joining walls of the wetting box to minimize leaking. Within

https://doi.org/10.1017/jfm.2014.110 Published online by Cambridge University Press

the wetting box, an interior plate is positioned with adjustable supports (not shown) that connect to the base of the apparatus. Shims (Precision Brand®) are used to set the distance between interior and support plates. The system is aligned such that the substrate's width narrowly fits between shims placed at opposite edges of the wetting box (see figure 3*c*). The confinement gap H shown in figure 3(*b*) results from the difference between the shim and tape thickness. The wetting region is left unconfined when the interior plate is completely removed from the system (this geometry will be denoted as $H \to \infty$).

The back wall of the wetting box includes liquid and air inlets. Liquid feed fills the vessel to a desired volume (usually 300 ml) prior to experimentation. During operation, compressed air enters the wetting box through the air inlet and pressurizes the liquid relative to atmospheric pressure P_{atm}. Liquid pressurization allows the meniscus to be positioned within the confinement gap, resisting the substrate's tendency to drag the meniscus toward the exit slot. The applied pressure P_{app} is controlled with a screw valve (Speedaire®) and measured by a manometer (Dwyer® Slack Tube) when $P_{app} < 10$ kPa and a pressure gauge (Binks®) for $P_{app} > 10$ kPa. Note that all values of P_{app} reported herein represent the gauge pressure relative to atmospheric pressure. Pressurization is not necessary for unconfined studies ($H \to \infty$) because gravitational forces maintain a constant liquid level away from the DCL, preventing any major changes in the meniscus position during a single run.

The critical speed U^{crit} associated with air entrainment is determined by gradually increasing the tape speed until triangular air films form at the DCL. These air films appear suddenly and uniformly along the entire width of web when $U \geqslant U^{crit}$, resembling the sawtooth meniscus discussed in § 1. Figure 4 shows visualization of the transition from steady wetting (figure 4*a*) to air entrainment (figure 4*b*). Recorded images are analysed with the MATLAB Image Processing Toolbox™ to improve contrast of the DCL and measure features associated with the air entrainment events illustrated in figure 4(*c–e*). These measurements are discussed in more detail in § 4.

When imposing narrow confinement gaps ($H \leqslant 300$ μm), capillary forces cause the tape to be drawn toward and sometimes contact the interior plate prior to start-up of the substrate motion. It was found that a PET mask placed over the interior plate greatly reduces adhesive forces that otherwise result from this interaction (figure 5). Similar to findings from our prior work (Vandre *et al.* 2012), critical speeds appear to be independent of P_{app} when the meniscus is located in the gap formed between the mask and substrate (figure 5*a*). Wetting characteristics, including U^{crit}, become sensitive to changes in P_{app} when the meniscus is positioned near the mask corner (figure 5*b*). Owing to an effective pinning of the SCL at the corner, liquid pressurization changes the interface shape rather than simply translating the meniscus, as discussed in § 4.1.

Glycerol/water solutions were chosen for this study because of their Newtonian behaviour and low vapour pressure at room temperature. In addition, liquid viscosity is easily adjusted through dilution with deionized water or concentration with 99.7 % pure glycerol. For the cases presented here, solution viscosities span a range of 25–1000 cP, corresponding to compositions of approximately 75 and 99.7 % glycerol (by weight), respectively (Sheely 1932). We assume a density of $\rho \approx 1200$ kg m^{-3} for each solution when estimating the capillary length, $l_{cap} = \sqrt{\sigma/\rho g}$.

Experimental uncertainty arises from several different sources during each run. Viscosity measurements (DV-II Brookfield viscometer) typically show a standard deviation of 10 % for each value of μ, while surface tension (Krüss K10ST digital tensiometer) remains within the bounds of $\sigma = 65 \pm 2$ mN m^{-1}. Contact angle

https://doi.org/10.1017/jfm.2014.110 Published online by Cambridge University Press

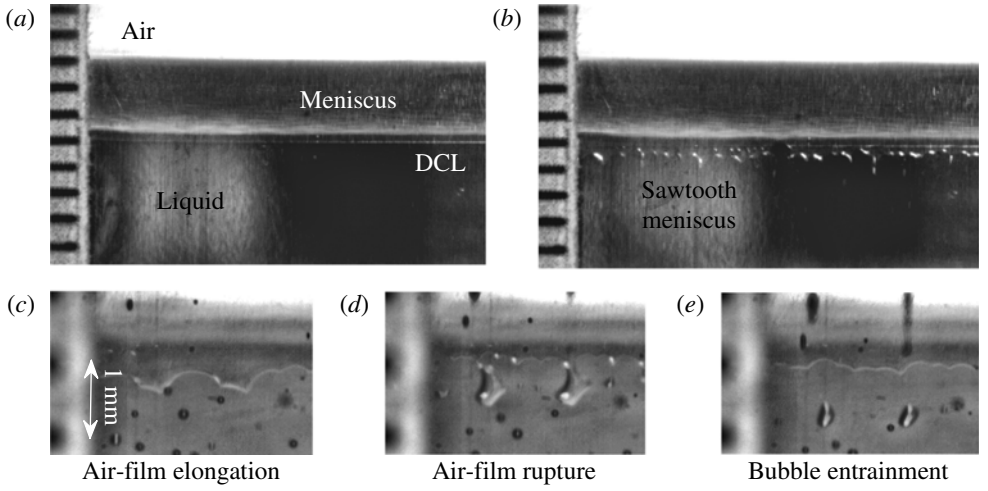


FIGURE 4. Visualizations of (*a*) steady wetting and (*b–e*) air entrainment recorded in the unconfined geometry ($H \to \infty$) with a high-viscosity glycerol/water solution ($\mu = 745$ cP). (*a*) The DCL appears smooth during steady wetting ($U \approx 0.055$ m s^{-1}), but (*b*) becomes serrated at the critical speed ($U^{crit} = 0.059$ m s^{-1}), forming a sawtooth meniscus. (*c*) Closer inspection reveals that air films of similar size and shape elongate from the DCL at U^{crit}. Over time, (*d*) air films become unstable and rupture, (*e*) leaving behind air bubbles that are entrained within the liquid flow. Note that ruler lines measure 1 mm distances in each image.

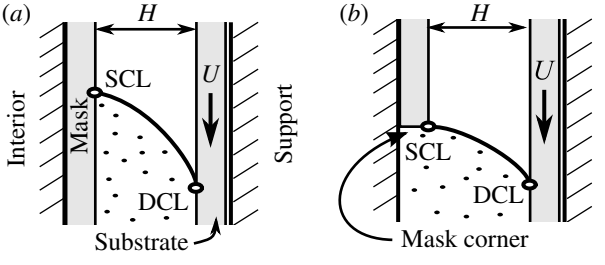


FIGURE 5. Illustration of the confined geometries used in this study. (*a*) The meniscus is confined within a parallel channel formed between interior and support plates. To prevent interaction with the substrate (see the description in the text), a PET mask covers the interior plate, forming a gap H between the mask and substrate surfaces. In this case, the SCL and DCL freely move in response to changing speed U or applied liquid pressure P_{app}. (*b*) In contrast, the meniscus remains effectively pinned when the SCL is located near the mask corner. Therefore, liquid pressurization alters the meniscus shape, as discussed in § 4.1.

hysteresis is observed on the PET substrate (Kruss DSA goniometer) with advancing and receding angles of approximately 80 and 65°, respectively. Substrate speed is held to within 0.005 m s^{-1} (Contrex® M-Drive controller) of the recorded set point U, producing relatively small errors in measured critical speeds ($U^{crit} > 0.05$ m s^{-1}) compared with the viscosity uncertainty. Other uncertainties include the reading of P_{app} (± 0.1 kPa and ± 2 kPa for the manometer and pressure gauge, respectively)

https://doi.org/10.1017/jfm.2014.110 Published online by Cambridge University Press

and the measurement of the gap H. Misalignment of the wetting-box walls and interior/supporting plates contributes the most significant error to the system. Although this error is difficult to quantify, passing shims of varying thickness through the gap reveals that this uncertainty is less than 50 μm for the values of H reported here.

3. Critical speeds

Air entrainment is observed above some critical substrate speed for all cases investigated in this study. As illustrated by figure 4, the DCL becomes three-dimensional and unsteady at U^{crit}, forming unstable air films that produce air bubbles upon rupture. Supercritical speeds ($U > U^{crit}$) tend to lengthen the air films and quicken rupture, although the dynamics depend strongly on the liquid viscosity, as discussed in § 4.

The critical capillary number $Ca^{crit} = \mu U^{crit}/\sigma$ relates the strength of viscous stresses from liquid flow ($\sim \mu U^{crit}/H$) to surface-tension forces ($\sim \sigma/H$) at the onset of air entrainment. Several experimental studies have shown the critical capillary number to increase weakly with higher liquid viscosities (Burley & Kennedy 1976; Gutoff & Kendrick 1982; Burley & Jolly 1984; Blake & Ruschak 1997; Cohu & Benkreira 1998; Benkreira & Khan 2008), following a power-law relationship similar to

$$Ca^{crit} \approx K\mu^{0.258}. \tag{3.1}$$

We adopt the correlation above as a fitting function in order to efficiently compare the results of the current study with prior work. In general, we find good agreement between our measurements of Ca^{crit} for various glycerol/water solutions and (3.1). Unlike prior studies, we show that the coefficient K depends on properties of confined geometries, such as the gap width (§ 3.1) and liquid pressure (§ 3.2). We note that a more general form of (3.1) would involve the ratio of the viscosities of the advancing and receding phases (Kistler 1993). However, when the receding phase is air, the air viscosity is typically absorbed into the coefficient K, as is done in (3.1). Nevertheless, it is important to note that the viscosity ratio plays a key role in governing dynamic wetting failure even when the viscosity of the receding phase is much less than that of the advancing phase (Vandre *et al.* 2013).

3.1. *Confinement*

Our prior work showed that confinement delays the onset of air entrainment during dynamic wetting of a roll substrate with a single glycerol solution ($\mu \approx 120$ cP) (Vandre *et al.* 2012). The current study expands upon this result, demonstrating that narrow gaps increase the value of Ca^{crit} for glycerol/water solutions that span a wide viscosity range, as shown in figure 6(*a*). Furthermore, the tape substrate enters the wetting box completely dry, avoiding prewetting effects that may have influenced air entrainment in the previous system.

Although critical speeds depend on the liquid viscosity, the relative effect of confinement is nearly independent of μ. In other words, each data set (for fixed H) in figure 6(*a*) shows roughly the same power-law dependence on μ. Decreasing H shifts curves to higher Ca^{crit} values, changing the coefficient K in (3.1); fitted values of K are listed in table 1. (See the supplementary data available at http://dx.doi.org/10.1017/jfm.2014.110 for further discussion about the fits of (3.1) to the Ca^{crit} data in figure 6*a*.)

https://doi.org/10.1017/jfm.2014.110 Published online by Cambridge University Press

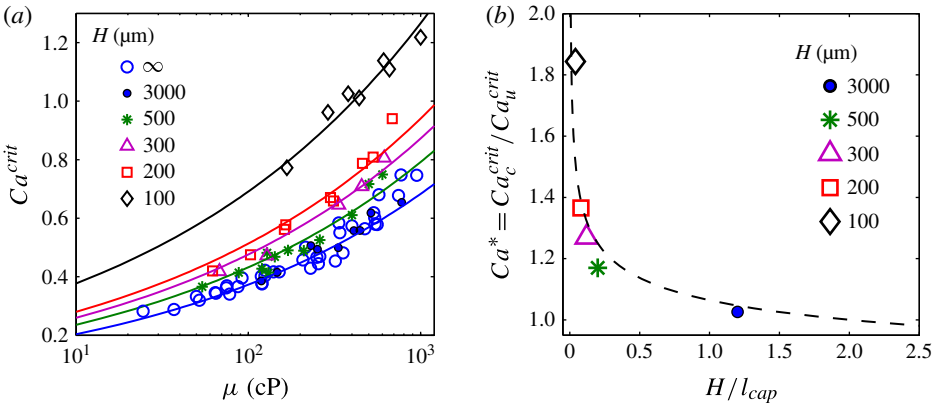


FIGURE 6. (Colour online) (*a*) Critical speeds plotted as function of μ for various confinement gaps H. Symbols (and colours online) denote the value of H for each data point, as listed in the legend. Bold lines are fitted to data sets of corresponding symbol shade (colour online) using (3.1) and K values listed in table 1. (*b*) The fractional increase in critical speed Ca^* is plotted against the dimensionless gap where $l_{cap} = 2.5$ mm. Each data point represents the ratio $Ca^* = K_c/K_u$, where K_u and K_c are the coefficients in table 1 for $H \to \infty$ and finite H, respectively. (See the text for further discussion.) The dashed line denotes (3.2), which was used to fit experimental data in a prior study (Vandre *et al.* 2012), with $l_{slip} = 200$ nm.

H (μm)	K (cP)$^{-0.258}$
∞	0.115
3000	0.118
500	0.132
300	0.146
200	0.157
100	0.212

TABLE 1. Coefficient values (K) used to fit (3.1) to Ca^{crit} data measured with various confinement gaps H.

Confinement effectively augments critical speeds measured in unconfined geometries (Ca_u^{crit}; $H \to \infty$) by some factor that depends on H. Therefore, $Ca^* = Ca_c^{crit}/Ca_u^{crit}$ represents the fractional increase in the critical speed (due to confinement) while holding all other parameters fixed, where Ca_c^{crit} is measured in the confined geometry with gap H. Since H only influences the coefficient in (3.1), Ca^* is independent of liquid viscosity and is simply defined by the ratio of K values from confined (K_c) and unconfined (K_u) systems: $Ca^* \approx K_c/K_u$. Figure 6(*b*) plots Ca^* for each value of H using the coefficients listed in table 1.

Despite differences in the experimental systems, figure 6(*b*) demonstrates that critical speeds follow the scaling obtained in our previous study (Vandre *et al.* 2012)

$$Ca^* \sim [\ln(H/l_{slip})]^{-1}, \tag{3.2}$$

where the slip length l_{slip} is related to the size of the region near the DCL where microscopic physics dominate the wetting mechanics. For the purposes of this study,

https://doi.org/10.1017/jfm.2014.110 Published online by Cambridge University Press

the slip length acts as a fitting parameter in (3.2) (Vandre *et al.* 2012), although there have been many experimental and theoretical investigations into the effect of l_{slip} on similar systems (Dussan V. 1976; Lauga, Brenner & Stone 2005; Neto *et al.* 2005; van Lengerich & Steen 2012). The scaling in (3.2) describes the trend of the data set in figure 6(*b*) with fair accuracy when using a fit of $l_{slip} = 200$ nm. A prefactor of $\ln(2l_{cap}/l_{slip})$ is selected when fitting (3.2) to experimental data, where l_{cap} is the capillary length ($l_{cap} \approx 2.5$ mm for glycerol). As discussed by Vandre *et al.* (2012), this prefactor reflects the fact that confinement only becomes important when gaps are less than the liquid's capillary length. Further decrease of H can significantly postpone the onset of air entrainment, leading to nearly a factor of two increase in Ca^{crit} when $H \sim 100$ μm.

3.2. *Liquid pressurization*

Liquid pressurization positions the meniscus within the confinement gap during dynamic wetting. Higher applied pressures P_{app} are needed as speed increases in order to resist substrate drag on the meniscus. (The online supplementary data suggest that P_{app} must increase linearly with Ca to hold the meniscus position steady.) The wetting box becomes susceptible to liquid and compressed-air leaks when $P_{app} > 10^4$ Pa. Since the pressure gradient in channel flow is inversely dependent on the square of the channel height (i.e. $P_{app} \propto H^{-2}$; see the supplementary data), high-speed wetting in gaps less than 100 μm could not be investigated in this study. Furthermore, only high-viscosity solutions ($\mu > 100$ cP) are used with the smallest gap ($H = 100$ μm) to limit the rate of liquid loss.

The onset of air entrainment appears insensitive to the magnitude of liquid pressurization when the meniscus is located within the gap (refer to figure 5*a*). In this case, increasing P_{app} moves the meniscus further up the gap, but does not significantly alter Ca^{crit} or the behaviour of the DCL. Consequently, critical speeds are reported as a single-valued function of liquid viscosity μ for each confinement gap H (see figure 6*a*).

This picture becomes more complicated when the meniscus is located at the leading edge of the gap. In this case, the meniscus does not freely move with increasing liquid pressures, but tends to remain fixed near the corner of the PET mask that covers the interior plate, as shown in figure 5(*b*). This effective pinning of the meniscus forces the air/liquid interface to change shape in response to pressurization (e.g. figure 11, as discussed in § 4.1).

While altering the interface shape, liquid pressurization also delays the onset of air entrainment, as illustrated in figure 7. Data points in figure 7(*a*) denote Ca^{crit} values recorded while pinning the meniscus at the mask corner. Under these conditions, higher liquid pressures promote steady wetting at faster speeds, resulting in multiple Ca^{crit} values for each glycerol solution. This pressurization effect yields significantly faster critical speeds than are obtained when simply confining the meniscus within the gap (see the bold curve in figure 7*a*). Since pressurization ceases to postpone air entrainment once the meniscus moves away from the mask corner, P_{app} must be carefully balanced with substrate drag to keep the SCL pinned. (Achieving this balance is difficult in practice, resulting in an apparent variation in the pressurization effect at different values of μ shown in figure 7*a*) In fact, figure 7(*b*) demonstrates that Ca^{crit} increases linearly with P_{app} until excessive liquid pressure causes the SCL to move along the mask. Larger gaps become prone to meniscus depinning at lower P_{app}, leading to less of an impact on the critical speed than the $H = 100$ μm case discussed above.

https://doi.org/10.1017/jfm.2014.110 Published online by Cambridge University Press

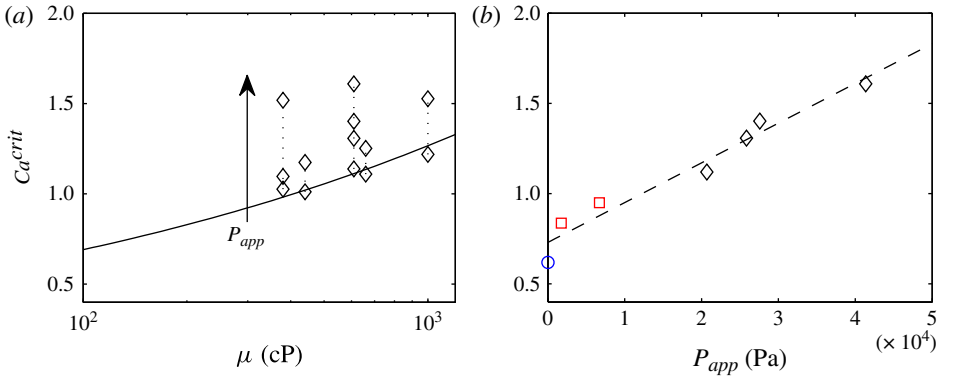


FIGURE 7. (Colour online) The effect of pressurization on Ca^{crit} when the meniscus is located at the mask corner (see figure 5*b*). (*a*) Critical capillary numbers plotted for various glycerol solutions with $H = 100$ μm. Each solution shows a trend of increasing Ca^{crit} with larger P_{app}. The bold line represents the power-law (3.1) fit for the $H = 100$ μm data set plotted in figure 6. (*b*) Critical speeds plotted as a function of P_{app} for $\mu = 600$ cP and $H = 200$ μm (square), 100 μm (diamond) and $H \to \infty$ (circle). Recall that unconfined wetting $H \to \infty$ does not require liquid pressurization, making $P_{app} = 0$ in this case.

4. Air-film characteristics

At the onset of air entrainment, thin air films elongate from the DCL, eventually rupturing and producing air bubbles that are captured within the wetting liquid. Figure 8 idealizes the three characteristic stages leading to air entrainment. First, the DCL adopts a serrated shape due to a periodic distribution of air films. Each air film resembles an isosceles triangle (figure 8*a*) of characteristic angle ψ formed by a base and side of lengths W and L, respectively. Second, perturbations cause the interface to rupture locally (figure 8*b*), releasing a portion of the air film with area A from the meniscus. Finally, surface-tension forces equilibrate the detached air patch, forming a spherical bubble with diameter D (figure 8*c*). The following sections discuss characteristics of the air-film shape (§ 4.1), thickness (§ 4.2), and rupture mechanism (§ 4.3).

4.1. *Shape*

System parameters strongly influence air-film size at the onset of air entrainment. With low-viscosity solutions ($\mu < 40$ cP), a single air film extends across the width of the substrate, pinning on the edges of the tape. In this case W is fixed by the substrate width ($W \approx 5$ cm), making the triangular shape completely specified by the angle ψ. Matching the observations of Blake & Ruschak (1979), ψ increases with faster substrate speeds ($U > U^{crit}$) in order to maintain some maximum velocity normal to the DCL (see the online supplementary data for further discussion).

Higher liquid viscosity decreases the width of the triangular air films, as demonstrated in figure 9. At relatively high viscosity ($\mu > 200$ cP), triangular air films are regularly distributed along the DCL forming the characteristic sawtooth meniscus. Fewer air films fit along the DCL (i.e. the width of the tape) in the moderate-viscosity regime (200 cP $> \mu >$ 50 cP), resulting in relatively straight portions of the DCL (figure 9*c*) in comparison with air entrainment in high-viscosity glycerol (figure 9*a*,*b*).

https://doi.org/10.1017/jfm.2014.110 Published online by Cambridge University Press

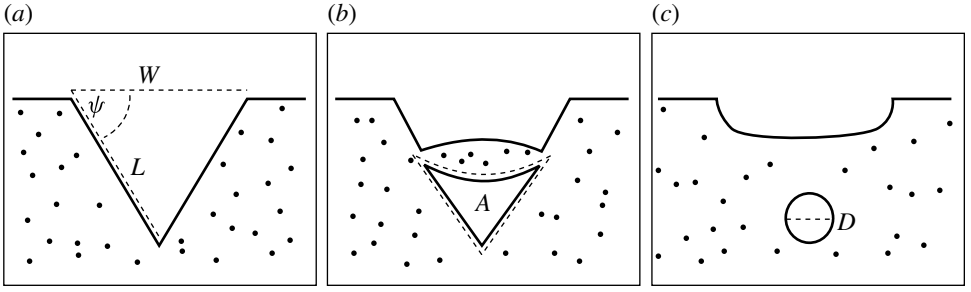


FIGURE 8. Idealization of the evolution of the air film during air entrainment. See the description in the text.

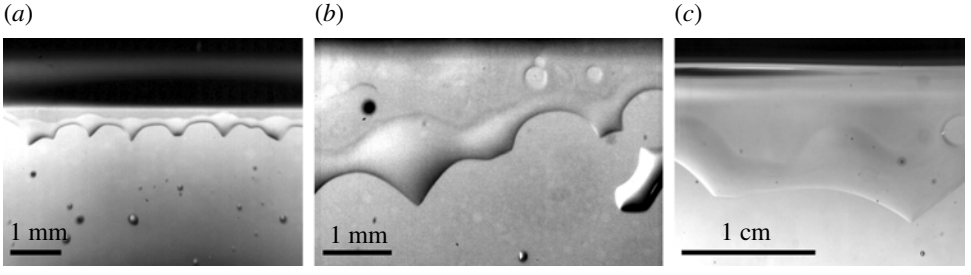


FIGURE 9. Visualization of triangular air films formed near the DCL at the onset of air entrainment with (*a*) $\mu = 1000$ cP, (*b*) 400 cP and (*c*) 75 cP for the unconfined geometry ($H \to \infty$).

Figure 10(*a*) plots the air-film width W (refer to figure 8*a*) measured at the onset of air entrainment as a function of liquid viscosity for the unconfined geometry (see the online supplementary data for details about the measurement of W). The data reflect a systematic decrease in air-film size as liquid viscosity increases, making W roughly proportional to $1/\mu$ (see the dashed line in figure 10*a*). As long as the air film remains small and avoids the tape edge, the angle ψ stays near 45° on average, independent of liquid viscosity. Supercritical substrate speeds ($U > U^{crit}$) generally lengthen the meniscus (including the air-film region), but also trigger faster rates of rupture and bubble entrainment. Qualitatively, air films appear to form sharper triangles as U increases beyond U^{crit}, but it is difficult to obtain meaningful measures of ψ due the rapid breakup of films into air bubbles. Note that ψ deviates from 45° for $\mu = 25$ cP in figure 10(*b*) due to the edge effects mentioned above.

Confinement alters the dynamics of air entrainment. For example, figures 11(*a*) and 11(*b*) show the rupture of air films with 400 cP glycerol for unconfined and confined geometries, respectively. As reflected by these images, confinement typically yields broad, irregular air films in comparison with the triangular shapes formed during unconfined air entrainment. This difference is caused by the volume of liquid displaced away from the DCL during elongation of the air film. In the confined case, displaced glycerol enters the narrow gap, where even small increases in liquid volume force upward movement of the SCL (see figure 5*a*). (Note that this is consistent with observations from prior work where a glycerol film was deposited on a confining surface during air entrainment (Vandre *et al.* 2012)). Through successive rupture and elongation of the air film, the SCL moves further away from the DCL, resulting in a broad air layer between the meniscus and substrate. Owing to the relatively large

https://doi.org/10.1017/jfm.2014.110 Published online by Cambridge University Press

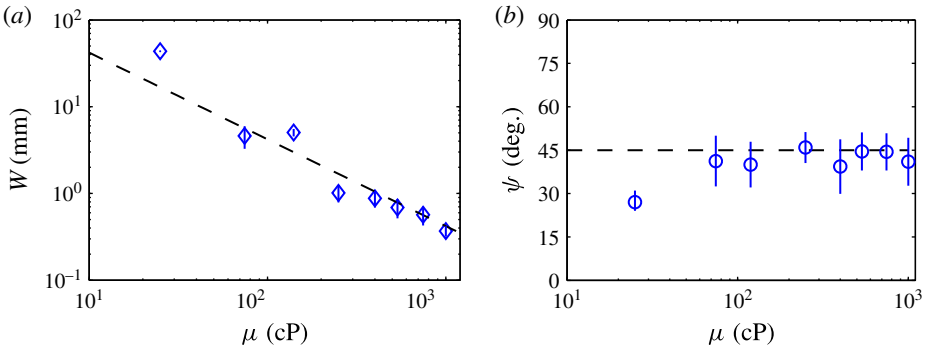


FIGURE 10. (Colour online) (*a*) The effect of liquid viscosity on air-film size as characterized by the width W of the triangular shapes formed at Ca^{crit}. (*b*) The angle ψ corresponding to the data points in (*a*).

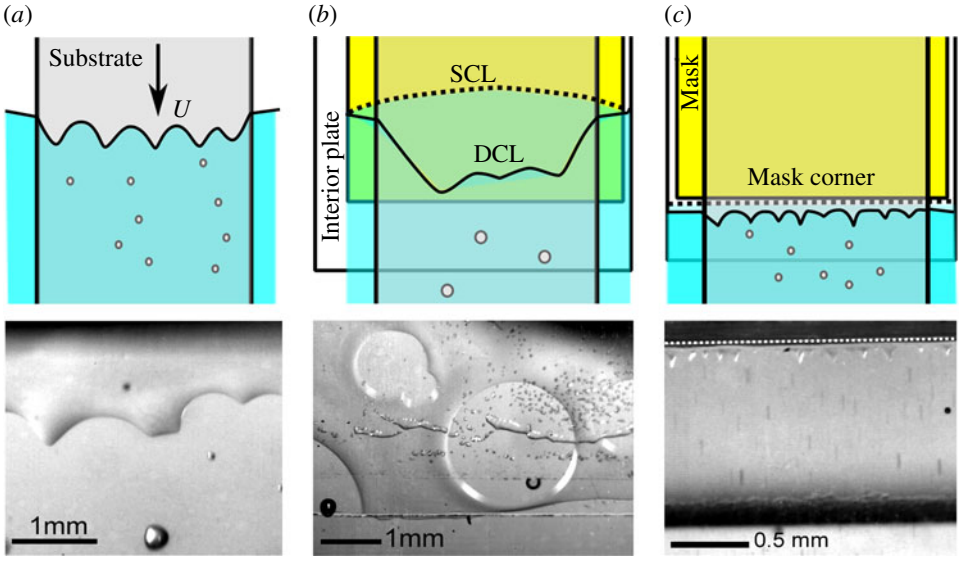


FIGURE 11. (Colour online) Visualization of the onset of air entrainment for (*a*) unconfined and (*b*,*c*) confined system geometries with $\mu = 400$ cP. Illustrations (top) idealize the system corresponding to each visualization image (bottom). (*b*) The SCL is located high above the DCL (outside of the visualization window) within the parallel channel of gap $H = 200$ μm ($P_{app} \approx 3$ kPa). (Note that the visualization shows bubbles trapped between the mask and interior glass plate.) (*c*) The SCL is pinned near the mask ridge with $H = 100$ μm and liquid pressurization ($P_{app} \approx 40$ kPa) reduces the size of the triangular air films. The mask ridge is marked with the white dashed line.

reservoir, liquid displaced during unconfined air entrainment negligibly impacts the liquid level (i.e. SCL position), allowing triangular air films with consistent size to form along the DCL.

Figure 11(*c*) demonstrates a considerable change in the air film when the meniscus is located near the mask corner. Although the meniscus is confined, the SCL remains fixed at the corner, preventing the formation of the broad air film discussed above.

https://doi.org/10.1017/jfm.2014.110 Published online by Cambridge University Press

While the meniscus remains effectively pinned, higher liquid pressure P_{app} decreases the scale of interface deformation, significantly reducing the size of triangular air films (see figure 11*c*) in comparison with the unconfined case (see figure 11*a*). Narrow gaps allow higher values of P_{app} before depinning the SCL (similar to observations of pressurized fibre coating (Ravinutala & Polymeropoulos 2002)), and much smaller air films are observed with $H = 100$ μm than in the other geometries reported in this study (additional visualizations are provided in the online supplementary data).

4.2. *Thickness*

Air-film thickness can be approximated from visualizations of the rupture events idealized in figure 8. During rupture, a mass of air separates from the DCL with volume $A \times h_f$, where h_f is the mean height of the air film defined by area A. The air mass forms a spherical bubble of diameter D as it becomes entrained within the liquid flow. Assuming that the volume of the air mass remains constant throughout this process, the film thickness can be estimated as

$$h_f = \frac{\pi D^3}{6A} \tag{4.1}$$

with A and D measured directly from visualization images. Previously, a similar method was used to estimate h_f with good precision during air entrainment in silicone oils (Marchand *et al.* 2012).

Using (4.1), air-film thicknesses are estimated at the onset of air entrainment with different solution viscosities in the unconfined geometry (figure 12). Similar to the trend of decreasing W with increasing μ (see figure 10*a*), the data in figure 12 show that increasing liquid viscosity thins the entrained air film. The air-film thickness is approximately $h_f \sim 10$ μm for high-viscosity liquids ($\mu \approx 1000$ cP) and increases by approximately an order of magnitude in the low-viscosity regime ($\mu < 50$ cP). Estimates from the glycerol/water system used in this study qualitatively match similar measurements made with silicone oils (Marchand *et al.* 2012), suggesting that the trend may be a general feature of air-entrainment systems. See the online supplementary data for further discussion of the image analysis techniques used to estimate h_f in this work.

It should be noted that the method of estimating h_f using (4.1) does not necessarily accurately reflect the actual thickness of the triangular air films along the DCL (see figure 8*a*). Prior to complete rupture, the interface enveloping the detaching air mass becomes more curved, making the thickness less uniform throughout the area A. Capillary forces resulting from the curved interface tend to squeeze air out of the mass and back into the continuous air phase above the meniscus. Furthermore, the triangular air films consistently show a thickness variation near the DCL resembling a capillary ridge (see figure 9). Considering all of these factors, it is difficult to know how estimates from (4.1) map onto the true air-film thickness profile that extends from the DCL to the outer meniscus. Nevertheless, a clear trend arises from the data plotted in figure 12, suggesting that this uncertainty does not obscure the dominant behaviour of air-film thickness as a function of μ.

4.3. *Rupture*

Rupture is initiated by a point of liquid–substrate contact that pierces through the air film. Figure 13(*a*) illustrates that multiple liquid contacts tend to simultaneously

https://doi.org/10.1017/jfm.2014.110 Published online by Cambridge University Press

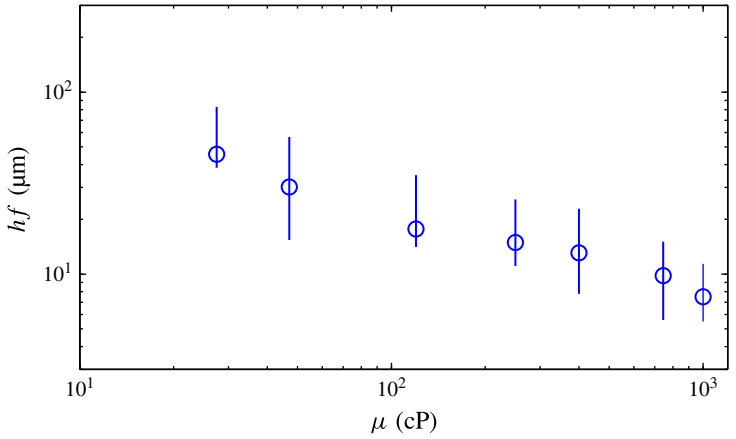


FIGURE 12. (Colour online) The effect of liquid viscosity on air-film thickness h_f measured at Ca^{crit} in the unconfined geometry ($H \to \infty$).

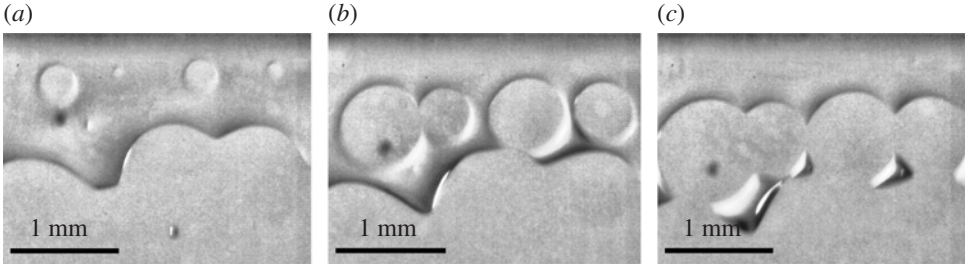


FIGURE 13. A sequence of visualizations showing the periodic nucleation of liquid contacts through the elongated air film, leading to film rupture and entrainment of air bubbles at Ca^{crit}. The images correspond to (*a*) 2 ms, (*b*) 5 ms and (*c*) 7 ms after the first point contact is observed. System parameters: $\mu = 400$ cP and $H \to \infty$.

nucleate just above the triangular air films. Once nucleated, these liquid sites grow rapidly as the rewetting rims advance downward at greater speeds than the substrate motion (see the online supplementary data). Despite becoming slightly elongated in the flow direction, the rewetting sites remain relatively circular in shape while increasing in size (figure 13*b*). Upon intersection with the DCL, the liquid sites trap air bubbles that become entrained in the liquid flow (figure 13*c*).

Variations in the air-film thickness are typically observed prior to the rupture events shown in figure 13. These thickness variations resemble wave crests moving perpendicular to the substrate velocity. Figure 14 demonstrates typical behaviour of these 'travelling waves' as they traverse the triangular air films. In this example, two visible waves separated by a distance l_0 travel from left to right with speed V, which approximately matches the substrate speed U (further discussion below). Note that waves are seen moving left-to-right and right-to-left at nearly the same frequency. Each wave remains inclined at an angle similar to ψ, suggesting that the initial thickness perturbation (that generates the travelling wave) arises during elongation of the triangular air film.

Figure 2 illustrates the complete rupture mechanism suggested from the observations of figures 13 and 14. At the critical substrate speed, air films form that are

https://doi.org/10.1017/jfm.2014.110 Published online by Cambridge University Press

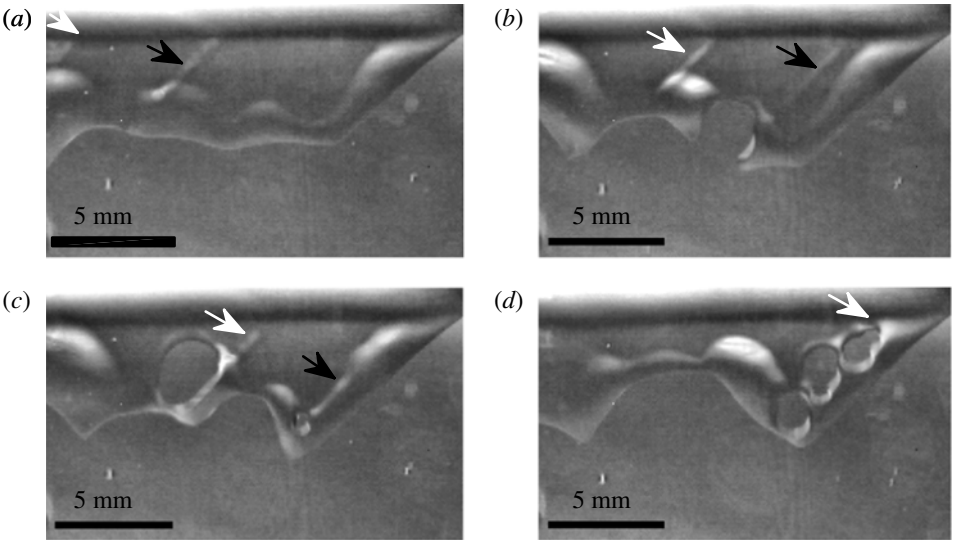


FIGURE 14. Visualization sequence illustrating thickness variations in air films leading to air-film rupture at Ca^{crit}. Two waves (denoted by white and black arrows) are shown moving from left to right at time (*a*) 0 ms, (*b*) 7.5 ms, (*c*) 10.0 ms and (*d*) 17.5 ms. System parameters: $\mu = 25$ cP and $H \to \infty$.

characterized by a thin region connected to a thicker capillary ridge near the DCL. Travelling waves perturb the interface, making the thinnest portion susceptible to break-up as long-range molecular forces initiate liquid contact with the substrate. Since perturbations are distributed along intervals of the wavelength, multiple liquid contacts nucleate simultaneously with periodic spacing characterized by a distance l_0. Substrate motion drives liquid toward the rupture site, growing the liquid contact until air bubbles are released from the DCL.

Each system used in this study shows signs of the rupture mechanism discussed above. For instance, each solution exhibits a characteristic wavelength l_0 associated with rupture, as demonstrated in figure 15 for the unconfined geometry. The data show that longer wavelengths (larger l_0) result during air entrainment in less viscous liquids. This trend holds until $l_0 \sim 5$ mm, at which point gravitational forces begin to level thickness variations along the interface (note that $l_{cap} \approx 2.5$ mm for glycerol), preventing further increase of l_0. Interestingly, the behaviour of l_0 closely matches the trend of decreasing W as μ increases (refer to § 4.1). Therefore, the size and distribution of triangular air films may be linked to the rupture mechanism that reshapes the DCL with periodic perturbations. The width W only significantly deviates from l_0 when a single air film spans the width of the substrate by pinning against the tape edges at $\mu = 25$ cP. This suggests that in addition to l_{cap} (which limits l_0 in the low-viscosity regime), some viscous length scale plays a significant role in determining the DCL shape. This viscous length scale is discussed in more detail in § 5.

5. Comparison with predictions from a hydrodynamic model

The behaviour of Ca^{crit} can be understood with insight gained from a hydrodynamic model for dynamic wetting failure. Governing equations and computational techniques

https://doi.org/10.1017/jfm.2014.110 Published online by Cambridge University Press

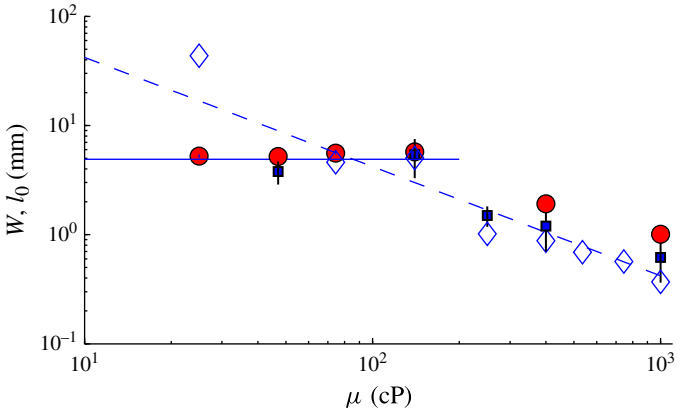


FIGURE 15. (Colour online) The perturbation wavelength l_0 observed at Ca^{crit} plotted against liquid viscosity. The distance l_0 is measured between travelling waves (circle) and nucleation sites (square) as illustrated in figure 2(*b*). The air-film width W (diamond) is also plotted for each case. The dashed line is taken from the fit of W in figure 10(*a*) and the solid line denotes $l_0 \approx 2l_{cap}$, where $l_{cap} = 2.5$ mm. Note that error bars lie within symbol margins when not shown.

for the model have been detailed in our prior work (Vandre *et al.* 2012, 2013), so here we provide only a brief overview. A Galerkin finite-element method is used to solve for 2D fluid displacement where an impenetrable air/liquid interface resides within a gap (H) between a stationary plate and a moving substrate. Creeping flow in both the liquid and air phases is assumed, and standard normal-stress, tangential-stress and kinematic conditions are applied at the air/liquid interface. The no-slip condition is imposed at the stationary plate, whereas a Navier-slip condition with slip length l_{slip} is applied along the moving substrate. In order to have a well-posed problem, microscopic contact angles are prescribed at the SCL and the DCL. Regardless of the value of the microscopic angle, viscous stresses bend the interface near the DCL, forming an 'apparent' contact angle that tends toward 180° as the capillary number approaches Ca^{crit}. For numerical convenience, we impose microscopic angles of 90° at the SCL and DCL, which is near the value of the advancing contact angle (≈80°) measured on PET. (Note that increasing the microscopic angle from 70 to 90° tends to change Ca^{crit} by less than 25 %. See Vandre *et al.* (2013) for further discussion.)

Flow fields obtained with the model show that strong pressure gradients pump the air flow away from the DCL during steady wetting. Liquid stresses deform the interface and restrict the air flow to a thin region between the interface and substrate until air stresses exceed the local capillary forces at some critical substrate speed, causing unsteady air entrainment. Decreasing the air viscosity μ_{air} relative to μ lessens the impact of the air stresses near the DCL, allowing for steady wetting at higher speeds. Figure 16(*a*) demonstrates that this trend of increasing Ca^{crit} with decreasing $\chi = \mu_{air}/\mu$ matches the power-law behaviour observed by experimentally varying the liquid viscosity.

Similar to experimental observations, the model predicts that critical speeds increase when the air/liquid meniscus is confined. Computed critical speeds are independent of the position of the meniscus within the channel created between the substrate and stationary surface. Therefore, matching observations from the experimental system,

https://doi.org/10.1017/jfm.2014.110 Published online by Cambridge University Press

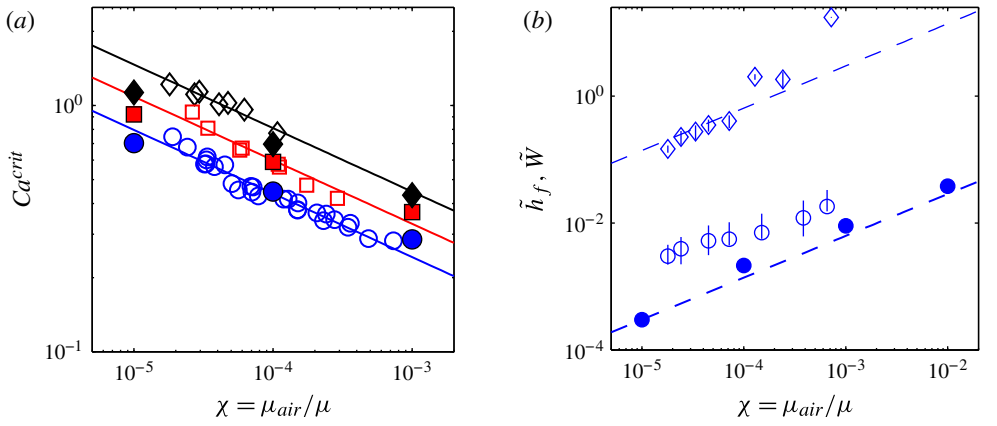


FIGURE 16. (Colour online) Comparison of experimental data with predictions from the 2D flow model (Vandre *et al.* 2012, 2013). (*a*) Critical capillary numbers measured as a function of the viscosity ratio $\chi = \mu_{air}/\mu$ for various confinement gaps H. Open symbols and solid lines are replotted from the experimental data in figure 6(*a*) assuming $\mu_{air} = 0.018$ cP (see H values in the legend of figure 6*a*). Closed symbols are calculated with the 2D flow model for $\lambda = l_{slip}/H = 5 \times 10^{-6}$ (circle), 5×10^{-5} (square) and 10^{-4} (diamond). (*b*) Air-film thickness (circle) and air-film width (diamond) plotted against the viscosity ratio. Experimental data (open symbols) taken from figure 10(*a*) and figure 12 are non-dimensionalized using glycerol's capillary length $l_{cap} \approx 2.5$ mm. Two-dimensional flow results (closed symbols) are computed at Ca^{crit} with $\lambda = 10^{-5}$. Dashed lines represent $h_f \propto \chi^{2/3}$.

there is a single value of Ca^{crit} for a given liquid (i.e. a given value of χ) confined within a parallel channel of gap H.

The degree of confinement is modelled with the parameter $\lambda = l_{slip}/H$, where l_{slip} is a small length scale ($l_{slip} \ll H$) associated with the magnitude of fluid slip along the substrate near the DCL. This microscale slip plays a more significant role as λ increases, reducing viscous bending of the interface and allowing for steady wetting at higher speeds. Similar to the scaling relationship in (3.2), predicted values of Ca^{crit} obey a logarithmic dependence on λ. Therefore, the choice of l_{slip} slightly influences the absolute value of the predicted critical speed, but does not change the dominant trends shown in figure 16(*a*). Using $l_{slip} = 10$ nm (as we have done for all of the calculations shown in figure 16), Ca^{crit} values predicted from the model come within 25 % of the experimentally measured critical speeds, showing significant improvement over the factor-of-two discrepancy found with our prior experimental system (Vandre *et al.* 2012). Although the confinement trend is consistent between our two experimental studies (e.g. figure 6*b*), the current study yields lower values for the critical speeds (for the same glycerol viscosity and confinement gap), providing better agreement with predictions from the model. Presumably, this improvement is due to the use of a dry PET substrate, which better matches the modelled substrate than the prewetted roll used in our previous experimental study.

It should be noted that matching the predictions of the 2D model to the experimental data produces a smaller slip length ($l_{slip} = 10$ nm) than that which is used with the scaling (3.2) in figure 6(*b*) ($l_{slip} = 200$ nm). Although experimental and theoretical studies suggest a broad range of feasible slip length values (e.g. $l_{slip} \sim$ 1 nm–10 μm in Lauga *et al.* (2005)), simple fluids on relatively smooth substrates

https://doi.org/10.1017/jfm.2014.110 Published online by Cambridge University Press

typically show $l_{slip} \sim$ 1–10 nm, which agrees well with the value used in the finite-element calculations. These findings are analogous to our prior work, where it was determined that the 2D model provides a better estimate of l_{slip} than a simplified analysis using lubrication theory (Vandre *et al.* 2012). Finally, we note that in order to match the model predictions to data from experiments in the unconfined system (figure 16), we have chosen $\lambda \approx l_{slip}/l_{cap}$. This reflects the fact that once the gap width H is comparable to the capillary length, confinement effects are no longer significant (Vandre *et al.* 2012).

Although pressurization effects are not directly studied with the model, similar trends are observed when a large body force is numerically imposed on a confined air/liquid meniscus (see the online supplementary data). The body force acts as a constant pressure gradient within the wetting liquid, pressurizing the liquid below the meniscus ($\sim P_{app}$) relative the air pressure ($\sim P_{atm}$) above. Higher liquid pressures force larger interface curvature, causing the meniscus to appear shorter as it only bends sharply on small scales close to the DCL. Owing to the sharp curvature, the interface supports large capillary stresses that postpone air entrainment to high substrate speeds. In reality, the cornered obstruction will generate a more complex pressure field than that modelled with a body force. However, qualitative agreement between the two cases suggests that a hydrodynamic model captures the essential mechanics of dynamic wetting near the onset of air entrainment.

In addition, experimental visualizations reveal interface characteristics at the onset of air entrainment that qualitatively match predictions from the model. Most notably, the elongated air films are thickest near the DCL (e.g. figure 9), resembling capillary ridges (see Vandre *et al.* (2013) for supporting data from the model). Similar behaviour is observed for the case of liquid-film withdrawal, in which a thick capillary wave forms at the dewetting contact line prior to complete entrainment (Snoeijer 2006), matching model predictions near steady-state bifurcation points (Delon *et al.* 2008). However, liquid films eventually elongate to a state of steady deposition (i.e. Landau–Levich film) (Maleki *et al.* 2007), whereas air films rapidly become unstable and rupture into bubbles. Although transient analysis would be needed to model bubble entrainment, steady-state predictions provide insight into the nature of the elongated air films prior to rupture.

The size of the air film may be determined by a local balance of capillary and viscous stresses. The hydrodynamic model shows that this viscocapillary balance crucially influences an interfacial inflection point in the vicinity of the DCL. The inflection-point height decreases exponentially with increasing Ca, sharpening interface curvature near the DCL to balance local capillary forces with the increasing viscous stress. Since Ca^{crit} increases with higher liquid viscosity, smaller inflection-point heights are computed at the onset of air entrainment with lower χ values. Figure 16(*b*) demonstrates that this trend resembles the behaviour of the experimental air-film thickness $\tilde{h}_f$, where the overbar denotes a dimensionless value. (Length is scaled by l_{cap} for the unconfined experimental systems, whereas the gap H is the characteristic length in the model since gravity is neglected.) Both the experimental and computational data reflect a weak power-law dependence on viscosity (approximately $h_f \propto \mu^{-2/3}$), although the origin of such behaviour is not yet completely understood. Figure 16(*b*) shows that this trend also describes the increase in air-film width W as viscosity decreases with the exception of the $\mu = 25$ cP case, where a single air film pins against the substrate edges. This suggests that the viscocapillary balance discussed above may influence the size of triangular air films

https://doi.org/10.1017/jfm.2014.110 Published online by Cambridge University Press

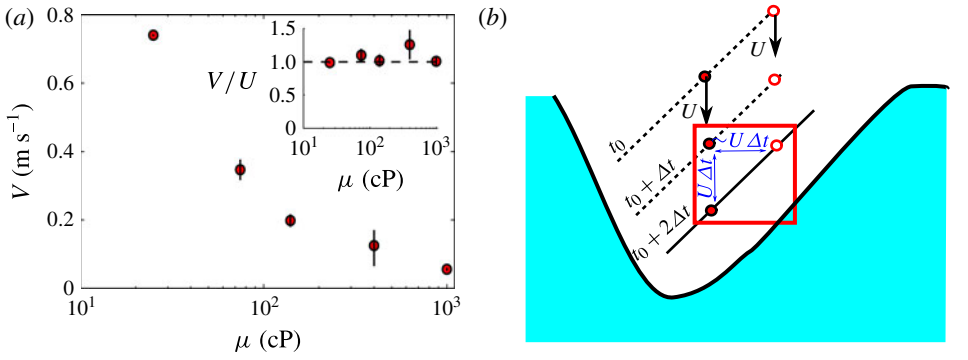


FIGURE 17. (Colour online) (*a*) Speed of wave propagation V measured at Ca^{crit} as a function of liquid viscosity for the unconfined geometry ($H \to \infty$). The inset shows V/U for each case and the dashed line marks $V/U = 1$. (*b*) Illustration of a wave moving with downward speed U at times t_0, $t_0 + \Delta t$, and $t_0 + 2\Delta t$. Owing to the 45° angle, a point along the wave may appear to move horizontally with speed $V \sim U$. However, this type of measurement actually accounts for two different points (closed versus open symbols) that both propagate vertically toward the DCL.

in addition to film thickness. However, it is not yet clear how this effect interacts with the length scale arising from the travelling wave perturbations discussed in § 4.3.

Air entrainment ultimately occurs when elongated air films are perturbed and break into bubbles. In the current system, these transient events are linked to travelling waves that traverse the thin air layer (see § 4.3). These waves appear to the translate laterally along the substrate (refer to figure 2) with speed V, plotted as a function of μ in figure 17(*a*). The data show that V approximately matches the substrate speed U for each case (see the inset of figure 17*a*), suggesting that thickness variations originate above the triangular air film and follow the substrate motion toward the DCL. Despite the downward-directed velocity, a single wave may seem to move laterally through the air film, as illustrated by figure 17(*b*). Two images recorded at times separated by Δt appear to show the wave translating a horizontal distance $\sim U\Delta t$, whereas the material point (see the circles (shown in red online) in figure 17*b*) actually moves vertically through the air film. Since the waves remain inclined at approximately 45° angles, horizontal and vertical components of velocity approximately match the substrate speed U. Further investigation of the local flow field and interface shape is required to gain insight into the mechanisms governing the period l_0 (see figures 2 and 15) of the wave disturbances and subsequent interface rupture which leads to air-bubble entrainment.

6. Conclusions

This work focuses on the onset of air entrainment resulting when a planar (tape) substrate enters a glycerol/water bath at some supercritical speed. Unlike steady wetting, which features a smooth air/liquid meniscus, air entrainment evolves from a jagged sawtooth meniscus that forms a serrated DCL at the substrate. In general, system parameters influence the critical speed and DCL shape associated with this transition.

Similar to prior work, experiments conducted in this study demonstrate that higher liquid viscosities (Kistler 1993) and more confined geometries (Vandre *et al.* 2012)

https://doi.org/10.1017/jfm.2014.110 Published online by Cambridge University Press

postpone air entrainment to higher critical capillary numbers Ca^{crit}. Expanding upon past results, the current work shows that confinement similarly affects a variety of glycerol/water solutions (50–1000 cP), yielding high substrate speeds that can be further increased when pressurizing the liquid. Pressurization is achieved by obstructing meniscus motion with a sharp corner (refer to figure 5*b*), such that higher pressures applied to the liquid reservoir lead to changes in the interface shape and wetting characteristics. Similar effects have been observed in high-speed fibre coating (Ravinutala & Polymeropoulos 2002; Simpkins & Kuck 2003). However, to the best of the authors' knowledge, this work presents the first experimental demonstration of air entrainment postponed by liquid pressurization in confined planar systems.

In addition, this work studies the shapes and dynamics of air films that form at the onset of wetting failure. For the first time, quantitative evidence is provided to support past observations (Burley & Kennedy 1976) that smaller triangular air films form in liquids with higher viscosity. Furthermore, we find that the air film is sensitive to properties of the system geometry. Qualitatively, broad ($\sim$1 mm) irregular air films form when the meniscus is confined between parallel surfaces, whereas small ($\sim$10 μm) triangular films appear when pressurizing the liquid with the meniscus pinned near a cornered surface. In each case, bubble entrainment results when spanwise variations in the air-film thickness nucleate liquid contacts that rupture the films. This mechanism of air entrainment is clearly documented by close visualization of the contact line, capturing the wave-like disturbances that drive the air-film instability.

Experimentally measured critical speeds compare favourably against predictions from a hydrodynamic model that we have developed in prior work (Vandre *et al.* 2012, 2013), suggesting that viscous effects in the air flow trigger the onset of air entrainment. Furthermore, flow visualizations indicate that air films form a capillary ridge near the DCL, also matching predictions from our model that have gone unnoticed prior to this study. More work is needed to understand transient air-film dynamics, including the instability that leads to air-bubble entrainment. This would require a three-dimensional analysis of the unsteady two-fluid flow, which presents significant computational challenges due to the need for adequate numerical resolution of flow near the contact line. Nevertheless, this work contributes to the fundamental understanding of air entrainment along planar substrates, motivating future investigations into the complex problem of air-film growth and rupture.

Acknowledgements

We are grateful to 3M^{TM} for their generous donation toward this research. In addition, we thank M. L. Pekurovsky and R. C. Moore for many helpful discussions, and W. J. Suszynski for his valuable contributions to the design and construction of the experimental apparatus. We acknowledge financial support from the Industrial Partnership for Research in Interfacial and Materials Engineering and the Donors of the American Chemical Society Petroleum Research Fund.

Supplementary data

Supplementary data are available at http://dx.doi.org/10.1017/jfm.2014.110.

REFERENCES

BENKREIRA, H. & IKIN, J. B. 2010 Dynamic wetting and gas viscosity effects. *Chem. Engng Sci.* **65**, 1790–1796.

https://doi.org/10.1017/jfm.2014.110 Published online by Cambridge University Press

BENKREIRA, H. & KHAN, M. I. 2008 Air entrainment in dip coating under reduced air pressures. *Chem. Engng Sci.* **63**, 448–459.

BLAKE, T. D. 2006 The physics of moving wetting lines. *J. Colloid Interface Sci.* **299**, 1–13.

BLAKE, T. D., CLARKE, A. & STATTERSFIELD, E. H. 2000 An investigation of electrostatic assist in dynamic wetting. *Langmuir* **16**, 2928–2935.

BLAKE, T. D., DOBSON, R. A. & RUSCHAK, K. J. 2004 Wetting at high capillary numbers. *J. Colloid Interface Sci.* **279**, 198–205.

BLAKE, T. D. & RUSCHAK, K. J. 1979 A maximum speed of wetting. *Nature* **282**, 489–491.

BLAKE, T. D. & RUSCHAK, K. J. 1997 Wetting: static and dynamic contact lines. In *Liquid Flim Coating* (ed. S. F. Kistler & P. M. Schweizer), pp. 63–97. Chapman & Hall.

BONN, D., EGGERS, J., INDEKEU, J., MEUNIER, J. & ROLLEY, E. 2009 Wetting and spreading. *Rev. Mod. Phys.* **81**, 739–805.

BURLEY, R. & JOLLY, R. P. S. 1984 Entrainment of air into liquids by a high speed continuous solid surface. *Chem. Engng Sci.* **39**, 1357–1372.

BURLEY, R. & KENNEDY, B. S. 1976 An experimental study of air entrainment at a solid/liquid/gas interface. *Chem. Engng Sci.* **31**, 901–911.

COHU, O. & BENKREIRA, H. 1998 Air entrainment in angled dip coating. *Chem. Engng Sci.* **53**, 533–540.

DE CONINCK, J. & BLAKE, T. D. 2008 Wetting and molecular dynamics simulations of simple liquids. *Annu. Rev. Mater. Res.* **38**, 1–22.

DE GENNES, P. G. 1985 Wetting: statics and dynamics. *Rev. Mod. Phys.* **57**, 827–863.

DELON, G., FERMIGIER, M., SNOEIJER, J. H. & ANDROTTI, B. 2008 Relaxation of a dewetting contact line. Part 2. Experiments. *J. Fluid Mech.* **604**, 55–75.

DUSSAN V., E. B. 1976 The moving contact line: the slip boundary condition. *J. Fluid Mech.* **77**, 665–684.

GUTOFF, E. B. & KENDRICK, C. E. 1982 Dynamic contact angles. *AIChE J.* **28**, 459–466.

JACQMIN, D. 2002 Very, very fast wetting. *J. Fluid Mech.* **455**, 347–358.

KISTLER, S. F. 1993 Hydrodynamics of wetting. In *Wettability* (ed. J. C. Berg), pp. 311–429. Marcel Dekker.

LAUGA, E., BRENNER, M. P. & STONE, H. A. 2005 Microfluidics: the no-slip boundary condition. In *Handbook of Experimental Fluid Dynamics* (ed. C. Tropea, J. F. Foss & A. Yarin), Springer.

MALEKI, M., REYSSAT, E., QUÉRÉ, D. & GOLESTANIAN, R. 2007 On the Landau–Levich transition. *Langmuir* **23**, 10116–10122.

MARCHAND, A., CHAN, T. S., SNOEIJER, J. H. & ANDREOTTI, B. 2012 Air entrainment by contact lines of a solid plate plunged into a viscous fluid. *Phys. Rev. Lett.* **108**, 204501.

NETO, C., EVAN, D. R., BONACCURSO, E., BUTT, H.-J. & CRAIG, V. S. J. 2005 Boundary slip in Newtonian liquids: a review of experimental studies. *Rep. Prog. Phys.* **68**, 2859–2897.

RAVINUTALA, S. & POLYMEROPOULOS, C. 2002 Entrance meniscus in a pressurized optical fiber coating applicator. *Exp. Therm. Fluid Sci.* **26**, 573–580.

SEVERTSON, Y. C. & AIDUN, C. K. 1996 Stability of two-layer stratified flow in inclined channels: applications to air entrainment in coating systems. *J. Fluid Mech.* **312**, 173–200.

SHEELY, M. L. 1932 Glycerol viscosity tables. *Ind. Engng Chem.* **24**, 1060–1064.

SHIKHMURZAEV, Y. D. 2008 *Capillary Flows with Forming Interfaces*. Chapman & Hall/CRC.

SIMPKINS, P. G. & KUCK, V. J. 2003 On air entrainment in coatings. *J. Colloid Interface Sci.* **263**, 562–571.

SNOEIJER, J. H. 2006 Free-surface flows with large slopes: beyond lubrication theory. *Phys. Fluids* **18**, 021701.

SNOEIJER, J. H. & ANDREOTTI, B. 2013 Moving contact lines: scales, regimes, and dynamical transitions. *Annu. Rev. Fluid Mech.* **45**, 269–292.

VANDRE, E., CARVALHO, M. S. & KUMAR, S. 2012 Delaying the onset of dynamic wetting failure through meniscus confinement. *J. Fluid Mech.* **707**, 496–520.

VANDRE, E., CARVALHO, M. S. & KUMAR, S. 2013 On the mechanism of wetting faluire during fluid displacement along a moving substrate. *Phys. Fluids* **25**, 102103.

https://doi.org/10.1017/jfm.2014.110 Published online by Cambridge University Press

VAN LENGERICH, H. B. & STEEN, P. H. 2012 Energy dissipation and the contact-line region of a spreading bridge. *J. Fluid Mech.* **703**, 111–141.

WEINSTEIN, S. J. & RUSCHAK, K. J. 2004 Coating flows. *Annu. Rev. Fluid Mech.* **36**, 29–53.

YAMAMURA, M. 2007 Assisted dynamic wetting in liquid coatings. *Colloids Surf.* A **311**, 55–60.

YUE, P. & FENG, J. J. 2011 Can diffuse-interface models quantitatively describe moving contact lines?. *Eur. Phys. J. Spec. Top.* **197**, 37–46.

https://doi.org/10.1017/jfm.2014.110 Published online by Cambridge University Press